Hyperspectral Infrared Imaging of HF(v, J) Chemiluminescence and Gain in Chemically Reacting Flowfields†

W. T. Rawlins,* D. B. Oakes, and S. J. Davis

Physical Sciences Inc., 20 New England Business Center, Andover, Massachusetts 01810

Received: March 5, 2007; In Final Form: April 9, 2007

This paper presents results from investigations of chemically reacting flowfields and optical gain profiles in HF chemical laser media by infrared hyperspectral imaging. Subsonic and supersonic chemiluminescent F + H_2 reacting flowfields, produced in high-fluence microwave-driven reactors, were imaged at a series of wavelengths, 2.6−3.1 μm, by a low-order, spectrally scanning Fabry−Perot interferometer mated to an infrared camera. The resulting hyperspectral data cubes define the spectral and spatial distributions of the emission. Spectrally resolved images at high spatial resolution were processed to determine spatial distributions of the excited-state concentrations of the product HF(v, J) molecules, as well as spatial distributions of small-signal gain on specific laser transitions. Additional high-resolution Fourier transform spectroscopy and spectral fitting analysis determined detailed excited-state distributions in the reacting flowfields. The measurements showed that energetic HF(v, J) state distributions were generated by both the supersonic and fast-flow subsonic mixing schemes. In particular, the subsonic reactor produced a spatially distributed field of inverted, near-nascent state populations, with small-signal gains near 2−3%/cm.

1. Introduction

Chemical lasers rely on exoergic chemical or energy transfer reactions to produce population inversions in the product species. To function efficiently, these systems must have rapid and effective mixing of the reagent gas streams. The reaction kinetics and mixing dynamics are highly coupled, so both spatial and spectral information are required for comprehensive diagnosis of the energetic medium. This is often extremely difficult, especially for infrared systems such as HF. The HF laser uses the exoergic reaction

$$F + H_2 \rightarrow H + HF(v \leq 3, J) \qquad (1)$$

to generate partial inversions between several rovibrational levels in different vibrational states. This results in lasing on several lines of the HF($\Delta v = 1$) fundamental band in the 2.5−3 μm spectral region, namely, the $v' = 1,2$ P-branch rotational lines: (v', J') → ($v' - 1$, $J' + 1$). These transitions are denoted as $P_{v'}(J' + 1)$. For high-power HF lasers, the relevant lines of interest are the $P_1(6) - P_1(9)$ and $P_2(5) - P_2(9)$ transitions.[1] Lasing can also be achieved on P-branch lines in the first overtone band, $\Delta v = 2$, near 1.3 μm. The development of high-efficiency HF laser systems requires advanced optical and spectroscopic techniques for diagnosing the reagent mixing field, to determine rotational and vibrational state populations and spatial distributions of the gain. This paper describes spatially resolved gain measurements by infrared hyperspectral imagery and by Fourier transform emission spectroscopy, for HF(v, J) generated by reaction 1 in subsonic and supersonic flow systems driven by a high-fluence microwave plasma jet.

The rate coefficient for reaction 1 is large, with a collision efficiency of ∼10% at room temperature. This means that the rate of product formation is limited by the mixing of the separate flow streams containing the reactant species. In addition, the excited states of HF(v, J) that are initially formed in the reaction are rapidly quenched by collisions with the surrounding species, including HF, the reactant species F and H_2, and the carrier gases. This imposes requirements for rapid and efficient mixing of the reagent streams and high-speed, low-pressure flows to reduce the quenching in the optical resonator volume. Consequently, there is a need to optically diagnose the mixing field near the reagent injection point to characterize the effectiveness and stability of the system. The hyperspectral imaging technique provides direct views of the spatially distributed, state-to-state emission intensities and gains within the radiating volume, and enables prompt evaluation of the chemical and optical performance.

2. Infrared Hyperspectral Imager

We have developed an adaptive infrared imaging spectrometer (AIRIS) for spectral imaging measurements at 2.6−3.1 μm and have applied it to observations of HF emission in laboratory subsonic and supersonic reacting flow fields. The AIRIS device combines the imaging capability of an infrared camera with the spectral scanning capability of a rapidly scanned, medium-resolution Fabry−Perot Etalon.[2] The instrument consists of a low-order Fabry−Perot Etalon coupled to an infrared focal plane array and optical collection system. An infrared camera views the emission through an imaging lens and Etalon as shown in Figure 1. The Etalon is operated at a low interference order, i.e., at a mirror separation (∼10−20 μm) which is a small integral multiple of the wavelength. Under these conditions, the central spot of the transmitted Airy pattern fills the detector array with a spatially continuous image of the scene at each wavelength, and the concentric Airy rings lie well off the optical axis.[2] This enables operation with a large aperture, up to ∼36 mm diameter, and correspondingly high throughput. The low-order operation also results in a relatively large free spectral

† Part of the special issue "M. C. Lin Festschrift".

* To whom correspondence should be addressed. Phone: 978-689-0003. Fax: 978-689-3232. E-mail: rawlins@psicorp.com.

10.1021/jp071786r CCC: $37.00
Published on Web 05/23/2007

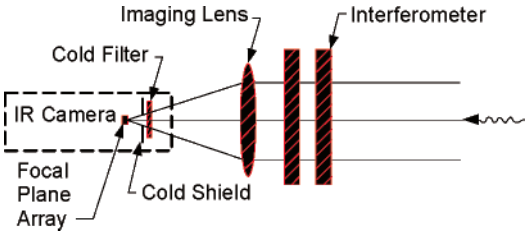

Figure 1. Schematic of hyperspectral infrared imager configuration.

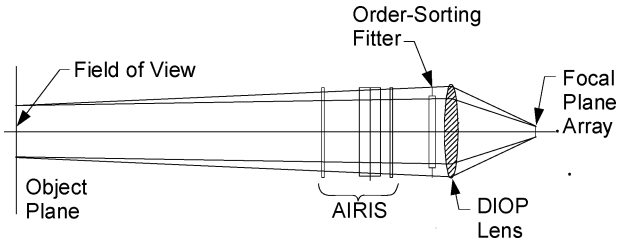

Figure 2. Schematic illustrating the optical configuration for the HF AIRIS instrument.

range between adjacent orders, so that bandpass interference filters can be used to isolate the free spectral range for a given order. Rapid, computer-controlled stepping of the Etalon through a series of pre-programmed wavelengths (or mirror spacings) produces a hyperspectral data cube containing images of the scene at each wavelength, over a short time frame (typically <1 s). These can be transformed into line-of-sight spectra of the emission intensity for each camera pixel's field of view. The spectral resolution is sufficient to permit spectral isolation and quantification of the key transitions. Absolute radiometric calibrations with a large-area blackbody radiation source are used to determine the pixel-by-pixel spectral responsivity of the instrument and convert the intensity data into absolute radiometric units (W/cm^2 sr μm). Analysis of response-corrected images of HF emission at a succession of wavelengths yields spatial distributions of the radiating HF(v, J) species in the reacting flowfield in which they are generated. Through application of the gain equation, we have extended this approach to produce spatial maps of population inversions and small-signal gains for specific transitions.

A schematic diagram of the HF AIRIS optical system is shown in Figure 2. The liquid-nitrogen-cooled InSb camera (Santa Barbara Focalplane) contains a 320 × 256 pixel array with 30 μm square pixels and no dead space. The camera is equipped with a 0.525 in. diameter cold stop 1.02 in. from the focal plane array (FPA), defining an f/2.3 field of view. A 3.5 μm short-pass cold filter (1 in. diameter) on the cold stop reduces thermal background radiance within the field of view, and thereby reduces the noise level of the system. The object plane is defined by a 50 mm compound lens (DIOP), f/2.3, mounted on a bayonet mount attached to the camera dewar housing. The lens is positioned to give a magnification of 1:20 for an object plane 91 cm (~36 in.) from the lens. This results in a rectangular object plane 19.2 cm wide × 15.36 cm high, with a pixel resolution element 0.6 mm square. A 1 in. diameter order-sorting filter (0.94 in. clear aperture) between the lens and the AIRIS unit reduces the overall transmission and throughput of the system but does not otherwise affect the magnification or image quality. The presence of the filter as a limiting stop ensures that the AIRIS mirrors are underfilled, i.e., that there are no stray rays which are not spectrally filtered by the Etalon. With the filter in place, the effective aperture stop of the system is f/3.85. The diffraction limit is given by 2.44λ(f/#) = 28 μm for

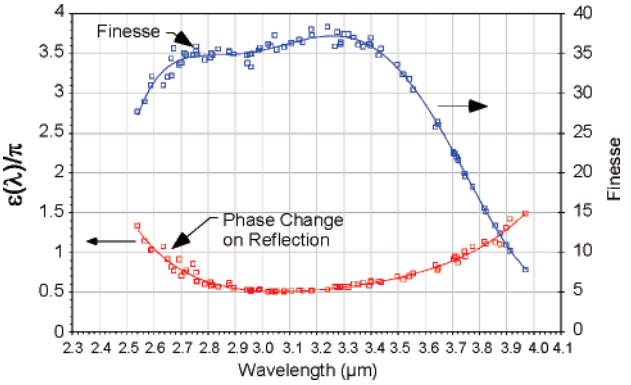

Figure 3. HF AIRIS Etalon finesse and phase change on reflection ($\epsilon(\lambda)/\pi$).

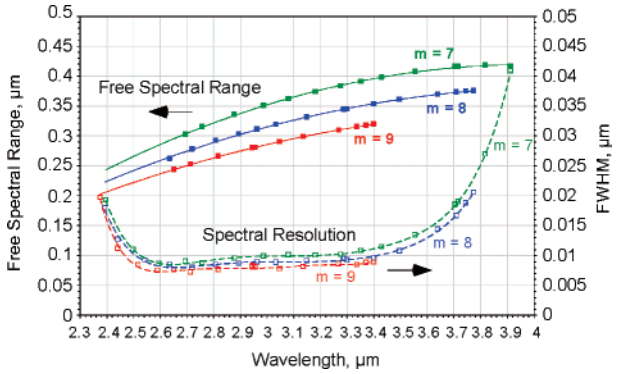

Figure 4. HF AIRIS Etalon free spectral range and spectral resolution (fwhm) for the seventh, eighth, and ninth orders.

λ = 3 μm. This is on the order of a pixel dimension, so there is only a slight degradation of the spatial resolution due to diffraction. Images of a Kodak resolution standard confirm a spatial resolution of 0.9 mm in the object plane.

The Etalon spacing and alignment are controlled by a computer-interfaced, four-point capacitance micrometry network. The scanning mirror is driven at high precision (~4 nm) by a set of three piezoelectrically actuated inchworm motors (Burleigh). Typical scan rates are 20 to 30 wavelengths/s. The Etalon is calibrated for wavelength and alignment by high-resolution measurements of the transmission fringes in an open-path Fourier transform infrared (FTIR) spectrometer. The wavelengths of the observed transmission peaks are fit to the Fabry−Perot resonance equations[2] to determine the Etalon finesse, phase change upon reflection, free spectral range, and spectral resolution (full width at half-maximum, fwhm). The finesse and phase data, shown in Figure 3, show the high-reflectivity operating range of the mirrors to be 2.6−3.6 μm. Over that wavelength range, the finesse is primarily limited by mirror flatness. The observed free spectral ranges and spectral resolutions, shown in Figure 4 for seventh, eighth, and ninth order, agree well with values predicted from the Etalon design specifications. The present measurements use eighth order for operation on HF emission, resulting in a spectral resolution of 0.008 μm. The wavelength accuracy of the Etalon, based on the FTIR calibration in eighth order, is <0.004 μm; fine-scale adjustment of the observed HF features to calculated line positions improves this value to 0.001 μm.

Two different filter combinations provide order-sorting filter options. Each combination consists of a bandpass and short-pass filter combined to define a wavelength range for eighth-order operation of the Etalon. Each pair of filters is mounted in

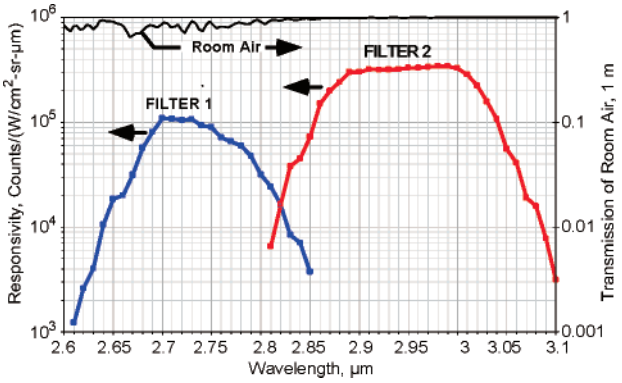

Figure 5. Field-averaged spectral responsivity of the HF AIRIS instrument. A computed room air transmission spectrum for a 1 m path is also shown (right-hand ordinate).

a six-position rotatable filter holder, which is positioned manually. One combination is a 2.6−3.4 μm bandpass filter and a 2.9 μm short-pass filter, which defines a range from approximately 2.6 to 2.85 μm for eighth-order operation without overlap from seventh and ninth orders. This range covers the $P_1(2-9)$, $P_2(1-6)$, and $P_3(1-2)$ transitions. The other combination is a 2.8−3.9 μm bandpass filter and a 3.1 μm short-pass filter, which defines the eighth-order operating range of approximately 2.8−3.1 μm. This wavelength range overlaps slightly with that of the other set, and covers the $P_1(8-12)$, $P_2(6-12)$, and $P_3(1-9)$ transitions.

The spectral responsivity of the fully integrated system, as measured for each order-sorting filter by blackbody calibrations, is shown in Figure 5. These curves were determined by observing the emission from a spatially uniform, large-area blackbody source at a known temperature, placed in the object plane of the lens. Also shown in the figure is a calculated transmission curve for 1 m of room air, illustrating the absorption due to room-ambient H_2O at the instrument's spectral resolution. The absorption effect is most pronounced at 2.65−2.75 μm. The observed responsivity curves include this absorption, so that correction of the HF emission spectra for the responsivity will, to first order, remove the effects of room air absorption from the data, provided the humidity of the air is similar for both the calibration and the HF measurements. For operation at 30 wavelengths/s, the instrument noise level is ~3 counts/pixel, corresponding to a noise-equivalent signal radiance (NESR) of $\sim 1 \times 10^{-5}$ W/cm^2 sr μm at 2.9 μm and $\sim 3 \times 10^{-5}$ W/cm^2 sr μm at 2.7 μm.

3. Chemical Production of HF(v, J) Emission

Reaction 1 was used to generate a reacting flowfield containing rovibrationally excited HF(v, J), by injecting H_2 into a flow of F atoms in both subsonic and supersonic flows. The F atoms were generated by an electrodeless, 2.6-kW discharge of flowing SF_6/He mixtures at ~1 atm in a high-power Microwave Driven Jet (MIDJet) device,[3] illustrated in Figure 6. The discharge gas mixture flowed through the high-pressure discharge chamber, where it was subjected to a high-power microwave-frequency discharge at 2450 MHz. The gas was injected into the chamber via a set of circumferentially mounted tangential jets, resulting in a swirl flow that confined the discharge plasma to a cylindrical volume near the axis of the system. The discharge effluent expanded through a water-cooled, conical nozzle into the downstream flow reactor section, where the optical measurements were made.

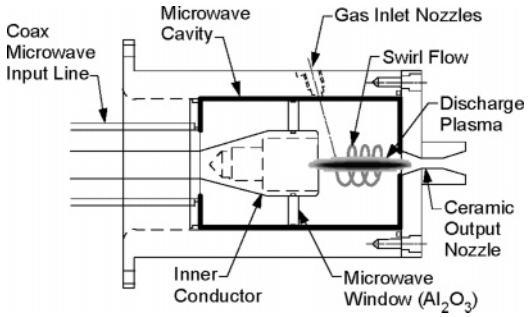

Figure 6. Schematic of MIDJet discharge chamber.

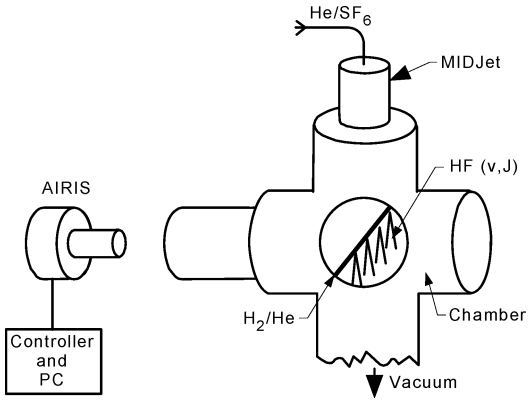

Figure 7. Subsonic reactor diagram illustrating MIDJet F-atom source, reagent injector, and AIRIS optical measurement system.

In the subsonic flow reactor, illustrated in Figure 7, the MIDJet discharge effluent passed through a supersonic nozzle and subsequent Mach disk, into subsonic flow through a large-volume interaction chamber at 2.6 Torr. On the basis of the equilibrium considerations of the power imparted to the gas, the estimated F-atom flow rate was ~6.7 mmol/s at a discharge temperature of ~1574 K. H_2/He mixtures were injected into the F-atom flow some 30 cm downstream of the MIDJet exit nozzle, where the flow was subsonic. The H_2/He injector was a 6 mm diameter stainless steel tube mounted orthogonally to the flow direction, with four in-line holes (0.5 mm diameter) spaced 1.5 cm apart. The injector assembly was water-cooled through an internal, coaxial 3 mm tube. Each of the four reagent injection orifices produced a flow of H_2/He which was supersonic from the exit plane to approximately 2 mm downstream and subsonic thereafter. The axes of the injected reagent flows were aligned with the direction of the main flow from the discharge. The experiments were performed with injectant flow rates of 0.4 and 8.9 mmol/s for H_2 and He, respectively. The estimated temperature in the mixing region was 700−800 K. The F-atom concentration was well in excess of the H_2 concentration, so HF was formed almost instantaneously as the two flow streams mixed. As illustrated in the figure, the AIRIS instrument was positioned to view the interaction region from the injector to about 9 cm downstream. This corresponded to a maximum reaction time of approximately 0.6−1 ms.

In the supersonic flow experiments, the H_2 reagent was injected directly into the supersonic F-atom flow from the MIDJet discharge, using the apparatus diagrammed in Figure 8. The apparatus includes an 8-in. long, 3-in. diameter stainless steel flow tube with a series of helium-purged optical ports providing optical access from 0.3 to 12 cm downstream of a water-cooled mixing nozzle. Typical pressures in the supersonic flow were 3−8 Torr, and were controlled by a conductance

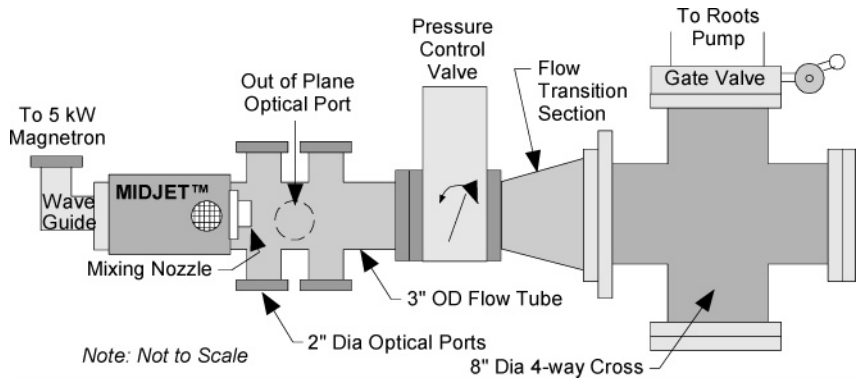

Figure 8. Schematic of the MIDJet supersonic HF flow reactor.

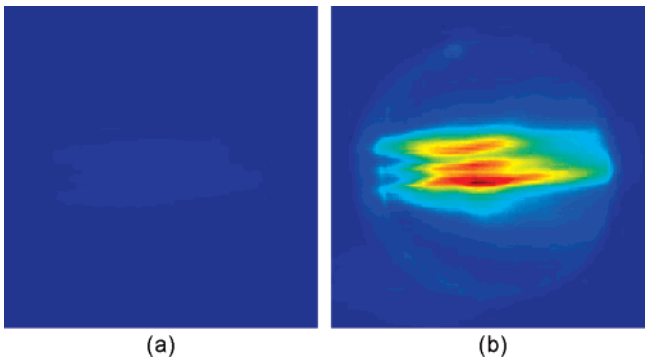

Figure 9. Images of supersonic HF flame for a MIDJet flow tube pressure of 8 Torr, spectral resolution 0.008 μm fwhm. (a) 2.650 μm. (b) 2.730 μm. Flow direction is from left to right.

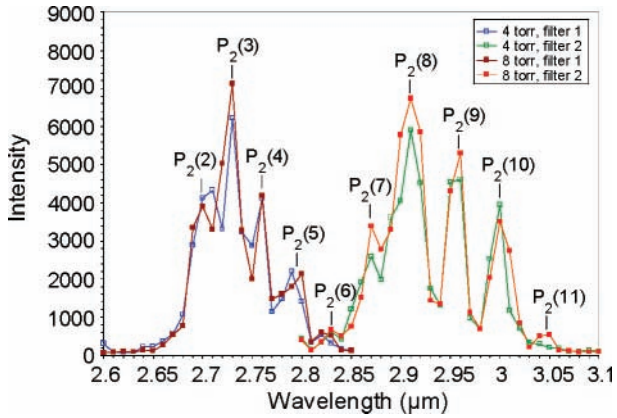

Figure 10. Survey scans of supersonic HF flame spectra for MIDJet flow pressures of 4 and 8 Torr, 0.01 μm wavelength interval, 0.008 μm spectral resolution. The spectral intensities are not corrected for spectral response. The locations of the $P_2(J'')$ features are indicated.

control valve. The conical mixing nozzle was fabricated from pyrolytic graphite, and coupled directly to the 2-mm aluminum nitride converging exit nozzle of the MIDJet to form a converging−diverging nozzle. The expansion cone had a 10° half-angle and an exit aperture of 6.5 mm. Four 0.5 mm diameter injector nozzles, spaced equally around the exit aperture of the main nozzle, injected H_2 into the supersonic exit flow, angled inward 20° with respect to the centerline. The AIRIS imager was positioned to observe the region immediately downstream of the injector exit plane, where the H_2 jets were mixing and reacting with the supersonic F-atom flow.

The observed raw images were corrected for background radiation by subtraction of an image obtained at a wavelength where no flame radiation can be observed. The background radiation removed in this manner consists of thermal radiation and reflections from hardware in the field of view, such as the exterior window flange, interior reactor surfaces, etc. No molecular infrared emission within the spectral bandpass could be detected in the F-atom flow. The background-corrected images were further corrected for the instrument spectral response by dividing the background-subtracted raw signal levels by the spectral responsivity data determined in the blackbody calibrations. The resulting processed images were expressed in absolute radiance units, W/(cm^2 sr μm), as a function of pixel horizontal and vertical coordinates, for each wavelength.

4. Spectral Images

Supersonic HF Flame. Spectral images from the supersonic HF flame at 8 Torr are shown in Figure 9. The flow direction is from left to right in each image. The image at 2.65 μm shows no flame radiation; this wavelength is isolated from HF lines by more than 2 spectral resolution elements in either direction and is near the short-wavelength transmission edge of the order-sorting filter combination. The image at 2.730 μm samples primarily emission from the $P_2(3)$ transition centered at 2.727 μm. The HF emission structure results from the mixing of the four H_2 jets with the supersonic F-atom flow, and appears in its 2-D projection as three flamelets spaced approximately 3 mm apart.

Spectra extracted from survey scans of the supersonic HF flames at 4 and 8 Torr are shown in Figure 10, for each of the two order-sorting filters. Each spectrum was extracted as the average of a small subset of pixels in the most intense region near the centroid of the lowest of the three lobes depicted in Figure 9b. The images were scanned with a wavelength interval of 0.01 μm, which is slightly larger than one spectral resolution element. This results in a relatively coarse spectrum, in which the detailed shapes of the individual spectral features are not fully delineated. These spectra have not been corrected for the spectral responsivity of the system, so the raw intensity distributions shown here should be used only for identification of the prominent features of the spectrum. In particular, the peak transmission of Filter 2 is about 2−2.5 times greater than that of Filter 1, resulting in pronounced exaggeration of the features at the longer wavelengths. The prominent features in the spectra are associated primarily with $P_2(J'')$ transitions, as indicated in the figure. Additional contributions to the underlying emission due to P_1 and R_3 transitions are likely but are not clearly identifiable in these spectra. More detailed scans, at wavelength intervals of 0.002 μm (four data points per resolution element), are shown in Figure 11. As with the survey scans, the spectra were extracted from the most intense region of the lowest

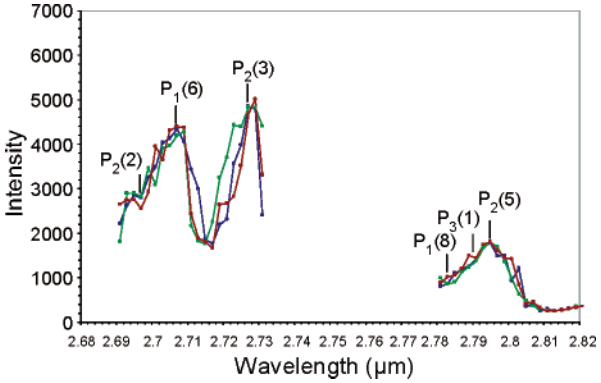

Figure 11. Supersonic HF flame spectra: spectral scans of the $P_2(5)$ and $P_1(6)$ regions at 0.002 μm wavelength intervals, 0.008 μm spectral resolution. The spectral intensities are not corrected for spectral response. The locations of the primary transitions are indicated.

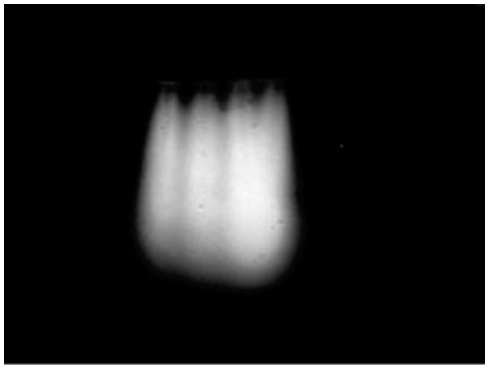

Figure 12. Processed image of emission from chemically produced HF($v = 2$, $J = 4$), $P_2(5)$ transition, 2.795 μm. The image frame measures 14.7 cm vertical × 19.6 cm horizontal. Flow direction is from top to bottom of the image.

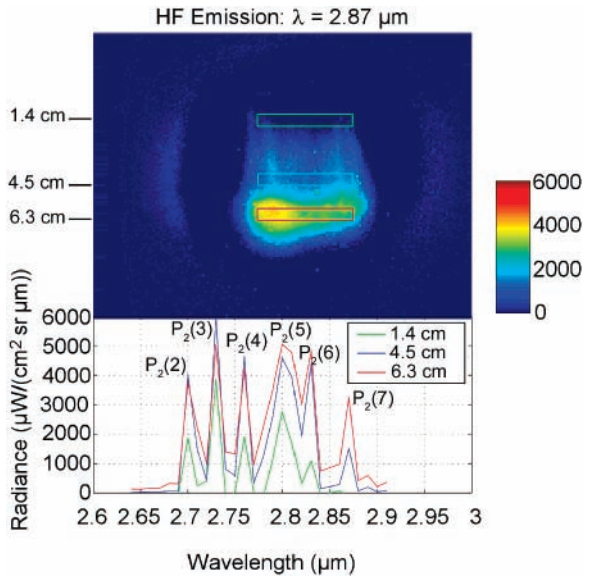

Figure 13. Processed image of HF($v' = 2$, $J' = 6$), $P_2(7)$ emission at 2.870 μm, and AIRIS spectra corresponding to the horizontal regions indicated on the image. Flow direction is from top to bottom of the image. The sampled horizontal strips are 0.6 cm high and are located downstream of the injector at distances of 1.4, 4.5, and 6.3 cm.

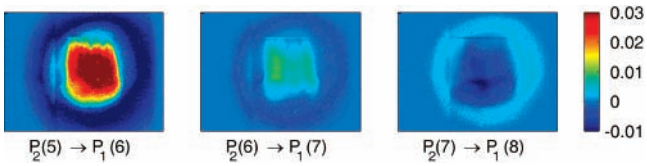

Figure 14. Image of small-signal gain observed for the HF $P_2(5)$, $P_2(6)$, and $P_2(7)$ transitions. Flow direction is from top to bottom of each image. Units of small-signal gain are cm^{-1}.

flamelet in Figure 9b, and are not corrected for spectral response. All three spectra in Figure 11 were obtained for the same MIDJet conditions, so comparison of the three provides an indication of the overall HF flame experimental and measurement reproducibility (~10−30%).

Subsonic HF Flame and Small-Signal Gain Images. A fully processed spectral image of HF emission from the $P_2(5)$ line (HF($v' = 2$, $J' = 4$)), at 2.795 μm, is shown in Figure 12. The flow direction in the image is from top to bottom. The faint horizontal line above the flame is reflected light from the injector tube. As the injected H_2 stream expands and mixes with the surrounding flow of F atoms, reaction 1 proceeds rapidly; prompt HF(v, J) emission appears within ~0.5 cm of the injection, and extends for at least some 9 cm downstream. The mixing of the F and H_2 flowfields is clearly evident in the image, both in the individual injectant jets and in the merging of the product flow streams beginning ~1 cm downstream of the injector. The emission intensity for HF($v = 2$, $J = 4$) passes through a maximum at intermediate flow distance and decreases near the bottom of the image due to the effects of collisional deactivation. Spectral intensity distributions extracted from three different flow distances are illustrated in Figure 13. The spectra were obtained at the relatively coarse wavelength spacing of 0.01 μm/step. The prominent features in the spectra are the $P_2(2-7)$ transitions. Less intense P_1 and P_3 transitions are also present but are not directly identifiable at this wavelength spacing. More detailed scans at 0.002 μm/step confirm the presence of these features. The prominence of the $v' = 2$ transitions indicates that a highly inverted vibrational population distribution is produced in the MIDJet reactor, likely resulting in significant small signal gain on some of the transitions.

Reaction 1 is known to produce HF(v, J) in state populations that are initially inverted, with most of the production occurring in $v' = 2$ and 3. As reaction time progresses, these initial populations cascade down into the lower states, resulting in increasingly relaxed state population distributions. Through examination of the spectral intensities of images like those in Figure 12, we can evaluate the spatial distribution of the small signal gain throughout the reacting flowfield. For an optically thin system at low pressures characteristic of Doppler broadened lines, the small signal gain for a given transition is given by

$$G = \frac{\lambda_0^3}{8\pi}\left(\frac{m}{2\pi kT}\right)^{1/2} A_{ul}\left(N_u - \frac{g_u}{g_l} N_l\right) \qquad (2)$$

where the subscripts u and l denote the upper and lower state of the transition, N_u and N_l denote the upper and lower state concentrations, A_{ul} is the Einstein coefficient for the transition, and the other symbols have their customary meanings. For the $P_2(5)$ transition, the number density of the upper state, N_u, is given by the ratio of the observed photon emission rate to the radiative rate for emission from the HF($v = 2$, $J = 4$) state. The lower state is HF($v = 1$, $J = 5$), for which the number density N_l can be obtained similarly, from the intensity of the $P_1(6)$ transition terminating in HF($v = 0$, $J = 6$). We observe images of the $P_1(6)$ emission at 2.707 μm. Thus N_u and N_l can be determined for every point in the image of the HF(v, J) flame

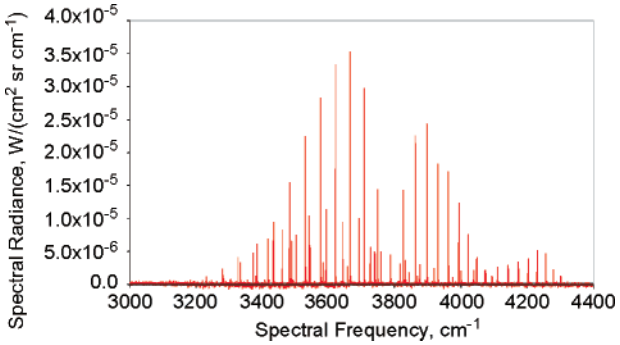

Figure 15. FTIR spectrum of HF(v, J) chemiluminescent emission from the F + H_2 interaction zone, averaged over the full field of view (no slit). Intensities are given in units of absolute radiance, W/(cm^2 sr cm^{-1}).

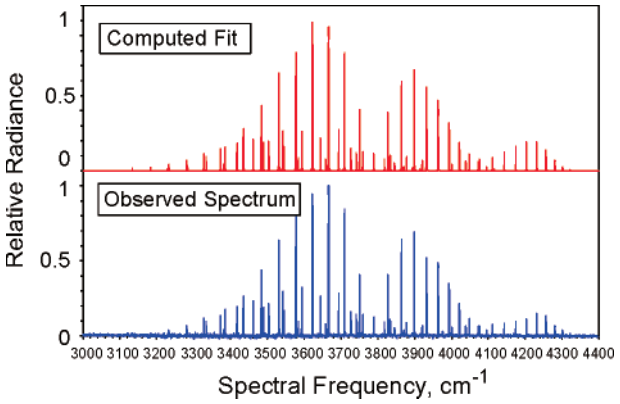

Figure 16. Observed and computed best fit spectra for the data of Figure 15. Intensities are normalized to unity at the highest experimental intensity.

and can be used to evaluate the small signal gain on the $P_2(5)$ transition. This is demonstrated by the images in Figure 14. For $P_2(5)$, the small signal gain is positive over most of the flame image, and is largest, 2−3%/cm, between 1.5 and 5 cm downstream of the injector. The gain maximum is also located below the middle two jets, where contributions from the neighboring jets enhance the mixing of the reactants. Similar analyses can be performed for other cascade transition pairs, e.g., $P_2(6)-P_1(7)$ and $P_2(7)-P_1(8)$ as shown in the figure. The $P_2(6)$ transition also exhibits positive gain, near 1%/cm; however, the $P_2(7)$ transition has negative gain throughout the image. Each of the transitions used in this analysis is isolated from its neighboring lines by at least one resolution element, so no corrections are required for overlapping transitions. This is borne out by FTIR spectra discussed below.

5. FTIR Spectroscopy

To evaluate HF(v, J) population distributions and small signal gains over the full range of the HF emission spectrum, we performed a detailed series of high-resolution spectroscopic measurements of the HF(v, J) emission in the subsonic and supersonic flames. These measurements employed a FTIR spectrometer, with a liquid-nitrogen-cooled InSb detector and a combination of 2.0 μm long-pass and 3.5 μm short-pass filters to eliminate short-wave radiation and to reduce radiometric noise from >300 K hardware in the field of view. The instrument was positioned similarly to the AIRIS instrument and viewed each HF flame with a collimated field of view ~5 cm in diameter. The absolute spectral responsivity of the FTIR

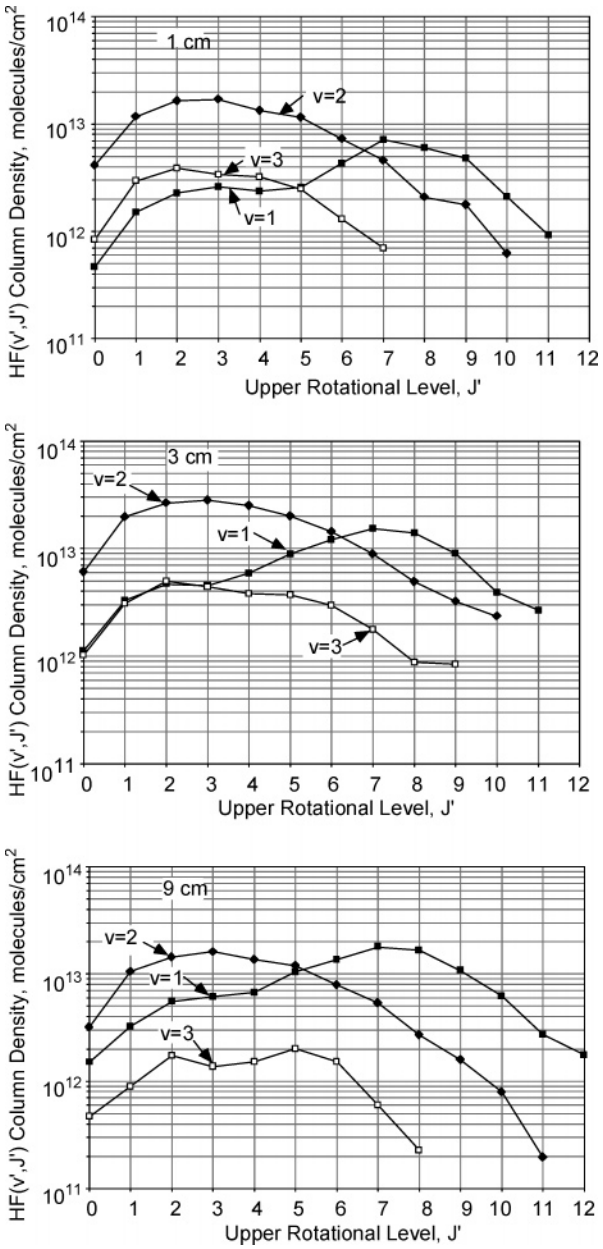

Figure 17. Path-integrated column densities of HF(v, J) 1, 3, and 9 cm downstream of the injector.

instrument was calibrated by measuring spectra of a blackbody radiance source with the same viewing geometry as for the flame measurements. The FTIR instrument was operated at a spectral resolution of 0.68 cm^{-1}, resulting in nearly complete resolution of each rotational line. The observed spectra were corrected for thermal background radiation and for spectral responsivity, to obtain absolute radiance units, W/(cm^2 sr cm^{-1}). The calibration also served to eliminate small absorption features due to room water vapor, since the blackbody source was placed at the same distance from the instrument as the window to the reaction chamber.

Subsonic HF Flame. For measurements of the subsonic flame, a horizontal slit aperture, 3 mm high and 6 cm long, was inserted into the chamber on a sliding probe, to permit masking of the field of view so that the flame could be viewed at specific distances downstream of the injector. This approach gave FTIR spectra of the horizontally averaged emission for different vertical distances 1−9 cm downstream of the injector and enabled observations of the evolution of the HF(v, J)

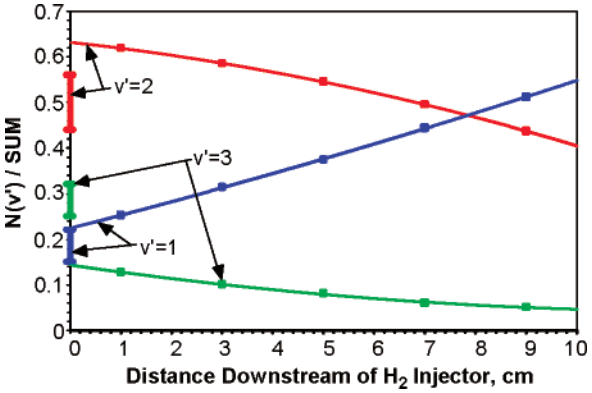

Figure 18. Subsonic HF flame: fraction of total population in each vibrational state. The bars on the ordinate indicate the range of experimental nascent vibrational distributions as reviewed in Reference 9.

state population distributions as a function of flow distance. An FTIR spectrum of the spatially averaged emission from the flame, as viewed without use of the slit mask, is shown in Figure 15. The spectrum exhibits R- and P-branch transitions from several rotational levels in each of the $v = 1$, 2, and 3 vibrational levels. Similar spectra were observed using the slit mask to isolate the emissions from different distances downstream of the injector.

We have applied a least-squares spectral fitting technique[4,5] to analyze the FTIR spectra quantitatively in terms of the excited species number densities in the reacting flowfield. This technique is based on the fundamental relationship between emission intensity and upper-state species number density[6]

$$R_i = hc\nu_i N_u A_{ul} \tag{3}$$

where R_i is the intensity of the ith rotation−vibration transition in W/cm^3 (integrated over the line). In practice, the emission spectrum of each HF(v, J) transition is computed using spectral line frequencies and Einstein coefficients calculated from spectroscopic first principles,[6] is convolved with the instrument spectral scanning function, and is fit to the calibrated spectra by a linear least-squares procedure to determine the upper state number densities. For HF, we used the spectral frequencies and Einstein coefficients computed by Setser and co-workers.[7] The FTIR instrument was operated with a triangular apodization, which results in a scan function of the form $(\sin X/X)^2$, where $X = 0.886\pi(\nu_i - \nu_0)/\Delta\nu$, ν_i is the frequency of the ith transition, and ν_0 and $\Delta\nu$ are the central frequency value and full width at half-height, respectively, of the instrument function. An example of a spectral fit to the experimental spectrum of Figure 15 is shown in Figure 16. The solutions to the least-squares fitting procedure are the path-integrated column densities of the radiating species. From inspection of the spectral images of the reaction zone, the approximate path length through the subsonic flame is 1.5 cm. The upper state column densities observed at 1, 3, and 9 cm downstream of the injector are shown in Figure 17. The evolution of the rotationally summed relative vibrational populations is shown in Figure 18. Near the injector, the fractional vibrational populations approach 0.22 for $v = 1$, 0.63 for $v = 2$, and 0.14 for $v = 3$. The generally accepted values for the nascent distribution from reaction 1 at room temperature are 0.00:0.15:0.55:0.30 for $v = 0-3$.[8,9] The ranges of reported nascent vibrational populations are illustrated in Figure 18 by the bars on the y axis. Our results for $v = 1$ and $v = 2$ are consistent with the expected nascent distributions, while the result for $v = 3$ is somewhat lower. Given the similarity of our

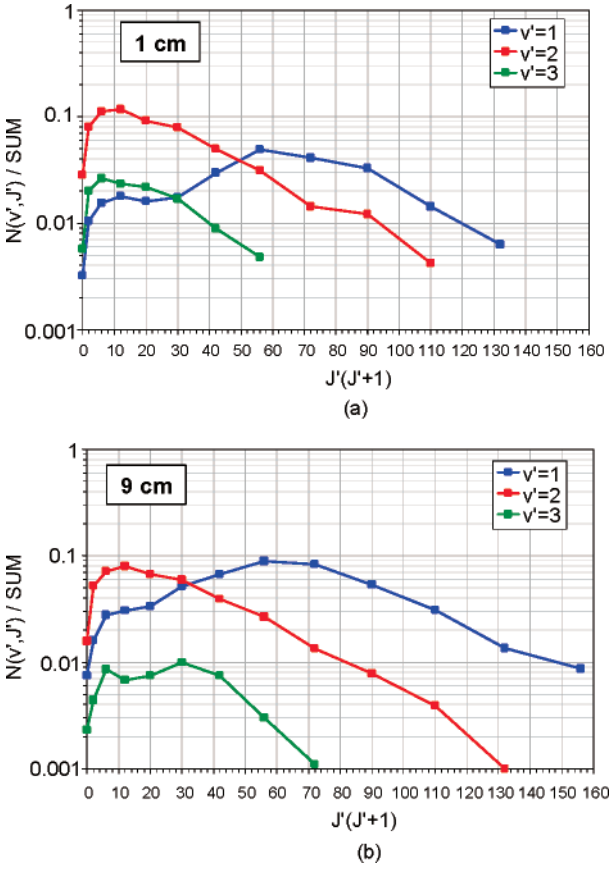

Figure 19. Rotational energy distributions for the data in Figure 17. (a) 1 cm downstream of the injector. (b) 9 cm downstream of the injector.

results at high collision energies to the nascent vibrational distribution for 300 K, it is likely that the vibrational distributions observed near the injector are at an early stage of partial relaxation, i.e., near-nascent, and that the $v = 0$ state is near zero population (at least for the lower rotational states). Further downstream in the reaction zone, the effects of collisional deactivation to deplete $v = 3$ and increase $v = 1$ populations are evident; however, the population in $v = 2$ remains high throughout.

The rotational distributions are highly non-Boltzmann, another indication of early stage product state distributions. Rotational temperature plots for the 1 and 9 cm cases are shown in Figure 19. For a Boltzmann population distribution, a plot of log(population) vs $J(J + 1)$ should give a straight line with negative slope proportional to a "temperature." Figure 19 shows some degree of thermalization for a few rotational levels; however, in general the population distributions are non-Boltzmann, even at the longest reaction time observed. The degree of rotational excitation is much greater than observed at room temperature,[10−13] probably as a result of our unique combination of translationally "hot" F-atoms and room-temperature H_2 molecules. In addition, Figures 17 and 19 show that the rotational population distributions undergo relatively small changes along the flow direction, even though the total vibrational populations clearly relax with increasing flow time as shown in Figure 18. This suggests that the rotational populations are in a quasi-steady state of production and deactivation along the length of the flame. The relative rotational populations are quite similar to those reported previously,[10−13] except those for $v = 3$ are somewhat broader. In particular, the $v = 1$ distributions are bimodal, with a second peak near $J = 7$, 8 which is strikingly similar to that observed

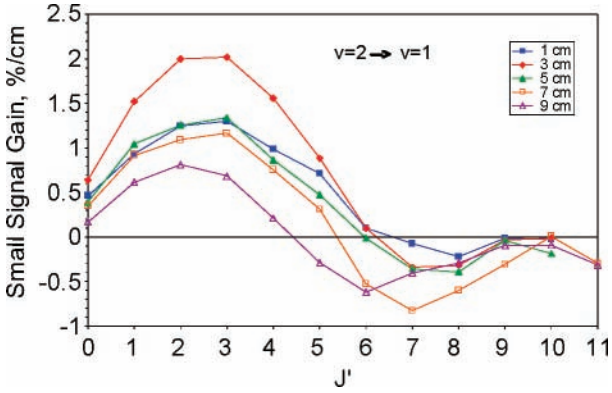

Figure 20. Small signal gains for the observed P-branch transitions for $v' = 2 \rightarrow v' = 1$ emission. Gains were determined for the indicated distances downstream of the injector.

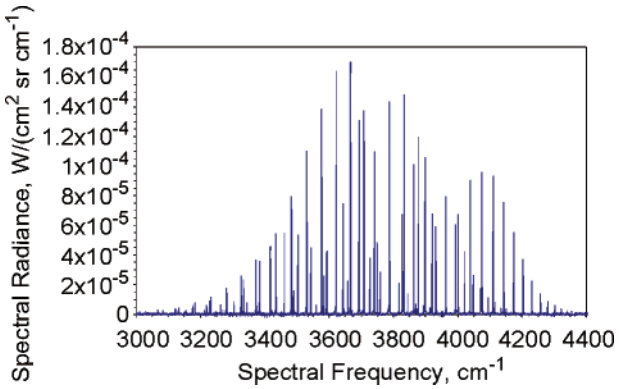

Figure 21. Supersonic HF flame: FTIR spectrum of HF(v, J) emission from the F + H_2 interaction zone, averaged over the full field of view, at 3 Torr flow pressure. Intensities are given in units of absolute radiance, $W/(cm^2\ sr\ cm^{-1})$.

by Polanyi and Woodall[10] at the same rotational levels. Those authors ascribed this secondary peak to a remnant of the true nascent rotational distribution for the F + H_2 reaction. Alternatively, the higher rotational states in $v = 1$ could be populated by collisional deactivation of $v = 2,3$ states via V → R, T energy transfer

$$\mathrm{HF}(v \geq 2, \text{low } J) + \mathrm{M} \rightarrow \mathrm{HF}(v = 1, \text{high } J) + \mathrm{M} \quad (4)$$

However, this process may be too slow to account for our observations at the shortest reaction times. Proper evaluation of the contribution of V → R, T transfer to the observed distributions requires a more detailed kinetics analysis. Nevertheless, the close similarity of the observed HF(v, J) relative populations to those of refs 10−13 is consistent with the production of near-nascent rovibrational distributions in the subsonic reactor.

The total amount of excited HF(v, J) is greatest at 3 cm downstream of the injector and decreases slightly with increasing distance. The average total HF(v, J) column density throughout the reaction zone is about $(2-3) \times 10^{14}$ molecules/cm^2. The column densities determined from the horizontally averaged FTIR spectra and from the spatially resolved AIRIS hyperspectral images are in good agreement.

Since the analysis of the FTIR spectra gives the full range of column densities in the three excited vibrational levels, we can determine the height-resolved small signal gains on all of the observed 2→1 and 3→2 transitions using eq 2 and assuming the path length through the flame is 1.5 cm. Gain values determined for the 2→1 P-branch transitions are shown in Figure 20. Gains for $J' = 0-4$ ($P_2(1-5)$) are positive throughout the observed reaction zone; the maximum of 2%/cm occurs for $J' = 2-3$ ($P_2(3,4)$) at 3 cm downstream of the injector. These results are in good agreement with the more detailed spatial distributions of gains shown in Figure 14. It is likely that the regions of high gain can be expanded or contracted by varying the momentum of the reagent H_2/He injection. It is also likely that lasing on some of the P_2 transitions can be achieved through placement of mirrors in the transverse dimension.

In contrast to the 2→1 transitions, all of the 3→2 transitions exhibit negative gain throughout the reaction zone. Although small signal gains on the 1→0 transitions cannot be directly determined because the concentration of HF in $v = 0$ is not measured, the values can be estimated for the shorter reaction distances assuming that the HF($v = 0$) concentration is negligible near the injector. For these conditions, the small signal gain is positive for all observed J, and the peak values at 1 and 3 cm are ~0.3 and ~0.8%/cm for $J' = 7-8$ ($P_1(8,9)$). At greater distances downstream of the injector, it is likely that the concentration of HF($v = 0$) builds up due to collisional deactivation, eventually resulting in negative gains.

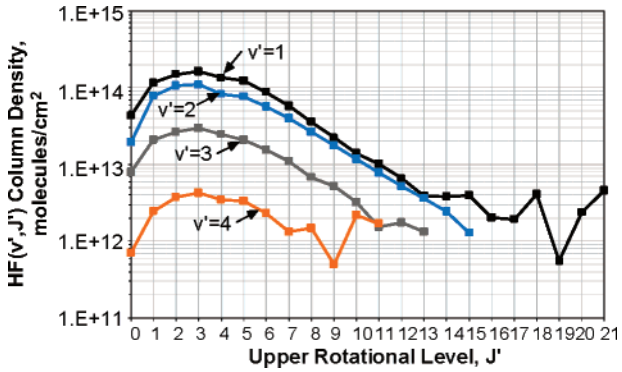

Figure 22. Supersonic HF flame: path-integrated column densities of HF(v, J).

The column densities from the spectral fitting can also be used to estimate small signal gains for the overtone transitions, 3→1 and 2→0. The $P_3(1-4)$ transitions all show positive gain at 1 cm downstream of the injector, with a maximum near 5×10^{-3} %/cm. If the HF($v = 0$) concentration is assumed to be negligible near the injector, the P_2 transitions are predicted to have positive small signal gain throughout the manifold, with maxima near 0.01 and 0.02%/cm for $J' = 2-3$ at 1 and 3 cm, respectively. These results are in general agreement with recent diode laser measurements of overtone HF gain reported by Wisniewski et al.,[14] who observed small signal gains on 2→0 transitions from 0.01 to 0.08%/cm.

Supersonic HF Flame. A typical FTIR spectrum of the spatially averaged supersonic flame at 3 Torr, observed with the same field of view as the hyperspectral images, is shown in Figure 21. This spectrum clearly exhibits significant population of the lower vibrational and rotational states characteristic of collisional deactivation. The HF(v, J) column densities determined by the spectral fitting procedure are shown in Figure 22. The vibrational populations decrease monotonically with increasing energy; however, it is noteworthy that several rotational states in $v' = 4$ are clearly present. For typical thermal collision energies, the overall exoergicity of the reaction is sufficient to populate only up to $v' = 3$.[10] The rotational populations for $J \geq 3$ exhibit Boltzmann-like distributions, i.e., exponentially decreasing with increasing $J'(J' + 1)$, with a characteristic

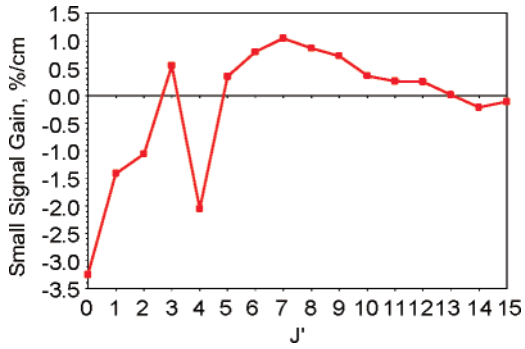

Figure 23. Supersonic HF flame: small-signal gains for the observed P-branch transitions for $v' = 2 \rightarrow v' = 1$ emission, 3 Torr flow pressure.

"temperature" of ~1340 K for all four vibrational levels. The populations for $J = 0,1,2$ in each vibrational level fall significantly below the Boltzmann fit. As a result of these distributions, the small-signal gains for the $v' = 2 \rightarrow v'' = 1$ transitions, shown in Figure 23, are considerably smaller than those observed for the subsonic flame. As illustrated in Figure 10, imager spectra at 4 and 8 Torr gave similar intensities and population distributions, suggesting that there is little pressure effect on the observed state populations over this range. Although the supersonic mixing case is expected to sample much shorter reaction times, the HF product state populations appear considerably more relaxed than the expected nascent distributions of reaction 1. In comparison, Manke et al.[15] reported similarly relaxed vibrational and rotational distributions for a supersonic HF laser system, including near-thermal Boltzmann rotational distributions.

6. Discussion and Conclusions

The method of hyperspectral infrared imaging of molecular emission provides a powerful optical diagnostic for probing complex chemically reacting flows with high spatial and moderate spectral resolution. The technique generates hyperspectral data cubes containing spatially resolved, two-dimensional images as functions of wavelength. Analysis of the data provides determinations of spatial maps of species concentrations, reagent mixing, and excited-state population distributions. The hyperspectral imaging diagnostic method can provide spatial profiles of small-signal gain in chemical laser cavities and can also be applied to measurements of the spectral and spatial profiles of HF laser beams as we have reported elsewhere.[16]

We have applied this technique to measurements of the reaction and mixing dynamics for an exoergic chemical reaction which is directly relevant to the HF chemical laser. The formation of excited HF(v, J) from the reaction of F with H_2 was investigated for both subsonic and supersonic flow systems, using a high-fluence microwave plasma jet to generate F atoms. Subsonic mixing of the reactants in a fast, high-temperature flow at 2.6 Torr generated inverted, near-nascent vibrational distributions and non-Boltzmann rotational distributions of excited HF(v, J) molecules, in a spatially distributed, largely unstructured mixing field. A combination of hyperspectral imaging and Fourier transform spectroscopy quantified the detailed, spatially resolved excited-state species concentrations and small signal gains, for mixing and reaction times ranging from ~0.1 to ~1 ms. HF(v, J) excitation was observed up to ($v' = 3$, $J' = 9$), consistent with the reaction exoergicity and the elevated thermal collision energies of the experiments. The total concentration of excited HF(v, J) in the reaction zone was $\sim 2 \times 10^{14}$ molecules/cm^3, corresponding to an HF(v, J) flow rate of roughly 30 μmol/s in a volume of ~100 cm^3. Positive small-signal gains were observed for the $P_2(1-6)$ transitions, with maxima of ~2−3%/cm for $P_2(3-5)$. These values are sufficient to produce lasing in the subsonic medium.

Mixing of the reactants in supersonic flow at 3−8 Torr also resulted in considerable HF(v, J) excitation; however, the observed vibrational and rotational populations were markedly different from those observed in subsonic flow. The data exhibit monotonically decreasing vibrational and Boltzmann-like rotational distributions; however, the excitation extends to much higher rotational states for each vibrational level, and excitation up to ($v' = 4$, $J' = 11$) is observed. This high degree of excitation appears to result from the high collision energies of the supersonic mixing field, where the directed flow velocities are well in excess of 10^5 cm/s. The vibrational and rotational populations exhibit considerably less "surprisal" than those observed in the subsonic flow case. In comparison to the subsonic mixing case, the supersonic population distributions resulted in lower small-signal gains which were maximized for higher rotational levels, i.e., ~1%/cm for $P_2(7-9)$.

These results for supersonic mixing might suggest a higher degree of collisional deactivation from the nascent distributions; however, the spectral images show little or no pressure effect on the spectral distributions. Since the observed reaction times for these conditions are <0.1 ms, i.e., much shorter than for the subsonic case, it is unlikely that the initial HF(v, J) distributions would be greatly altered, except perhaps by collisions with excess F at high velocities. Alternatively, the observed low-surprisal HF(v, J) distributions in the supersonic reacting flowfield may result directly from the reaction of F with H_2 at high collision energies and low impact parameters, resulting in a more statistical redistribution of the reaction energy in the products. The marked contrast between the subsonic and supersonic rovibrational population distributions is a significant and intriguing result. Further investigations would require systematic variations in pressure and reagent flow rates to explore a larger range of collisional coupling conditions.

Acknowledgment. We are grateful to the Air Force Research Laboratory Directed Energy Directorate, Kirtland AFB, NM, for support of this effort under Contracts F29601-01-C-0091 and F29601-02-C-0111. We also thank Dr. Gerald Manke II of AFRL for helpful discussions. A.M. Minhaj, D.X. Hammer, and S. Lee assisted with testing and data analysis.

References and Notes

(1) Gross, R. W. F.; Bott, J. F. *Handbook of Chemical Lasers*, John Wiley and Sons: New York, 1976.

(2) Marinelli, W. J.; Gittins, C. M.; Gelb, A. H.; Green, B. D. Tunable Fabry-Perot Etalon-Based Long-Wavelength Infrared Imaging Spectroradiometer. *Appl. Opt.* **1999**, *38*, p. 2594.

(3) Davis, S. J.; Oakes, D. B.; Read, M. J.; Gelb, A. H. Atomic Fluorine Source for Chemical Lasers. *Gas and Chemical Lasers and Intense Beam Applications III*; Davis, S. J., Heaven, M. C., Eds.; Proceedings of SPIE Vol. 4631 p. 178, January 2002.

(4) Rawlins, W. T.; Murphy, H. C.; Caledonia, G. E.; Kennealy, J. P.; Robert, F. X.; Corman, A.; Armstrong, R. A. COCHISE: Laboratory Studies of Atmospheric IR Chemiluminescence in a Cryogenic Environment. *Appl. Opt.* **1984**, *23*, 3316−3324.

(5) Rawlins, W. T.; Fraser, M. E.; Miller, S. M. Rovibrational Excitation of Nitric Oxide in the Reaction of O_2 with Metastable Atomic Nitrogen. *J. Phys. Chem.* **1989**, *93*, 1097−1107.

(6) Herzberg, G. *Molecular Spectra and Molecular Structure I. Spectra of Diatomic Molecules*; Van Nostrand: New York, 1951.

(7) Arunan, E.; Setser, D. W.; Ogilvie, J. F. Vibration-Rotational Einstein Coefficients for HF/DF and HCl/DCl. *J. Chem. Phys.* **1992**, *97*, 1734−1741.

(8) Cohen, N.; Bott, J. F. Review of Rate Data for Reactions of Interest in HF and DF Lasers. Report No. SD-TR-82-86, 1982.

(9) Manke, G. C., II; Hager, G. D. A Review of Recent Experiments and Calculations Relevant to the Kinetics of the HF Laser. *J. Phys. Chem. Ref. Data* **2001**, *30*, 713−733.

(10) Polanyi, J. C.; Woodall, K. B. Energy Distribution Among Reaction Products. VI. F + H_2, D_2. *J. Chem. Phys.* **1972**, *57*, 1574−1586.

(11) Chang, H. W.; Setser, D. W. Infrared Chemiluminescence and Energy Partitioning from the Reactions of Fluorine Atoms with the Primary Carbon-Hydrogen Bonds of Alkanes, Halogenated Methanes, and Tetramethyl Silane. *J. Chem. Phys.* **1973**, *58*, 2298−2309.

(12) Moehlmann, J. G.; McDonald, J. D. Infrared Chemiluminescence Investigation of the Abstraction Reactions Between Fluorine Atoms and Unsaturated Compounds. *J. Chem. Phys.* **1975**, *62*, 3061−3065.

(13) Chapman, W. B.; Blackmon, B. W.; Nesbitt, D. J. State-to-State Reactive Scattering of F + H_2 in Supersonic Jets: Nascent Rovibrational HF(v, J) Distributions via Direct IR Laser Absorption. *J. Chem. Phys.* **1997**, *107*, 8193−8196,.

(14) Wisniewski, C. F.; Manke, G. C., II; Hager, G. D.; Crowell, P. G.; Truman, C. R. Small Signal Gain Measurements in a Small Scale HF Overtone Laser. *Appl. Phys. A* **2003**, *77*, 337−342.

(15) Manke, G. C., II; Hewett, K. B.; Wisniewski, C. F.; Truman, C. R.; Hager, G. D. On the Presence of Rotational Nonequilibrium in a Supersonic HF Laser. *IEEE J. Quant. Elec.* **2003**, *39*, 1625−1634.

(16) Rawlins, W. T.; Oakes, D. B.; Mulhall, P. A.; Davis, S. J.; Wright, R. F.; Carroll, D. L.; Sentman, L. H. Advanced Optical Diagnostics for HF Laser Development. Paper AIAA 2002−2221, AIAA 33rd Plasmadynamics and Lasers Conference, Maui, HI, May 2002.